Supplemental Material for "Anharmonic Collective Oscillations and Gap Generation from Thermal Fluctuations in Isotropic Classical Spin Systems"

Anna Fancelli,[1,2] Matías G. Gonzalez,[1,2,3] Subhankar Khatua,[4,5,6] Bella Lake,[1,7] Michel J. P. Gingras,[4,8] Jeffrey G. Rau,[5] and Johannes Reuther[1,2]

[1]*Helmholtz-Zentrum Berlin für Materialien und Energie, Hahn-Meitner-Platz 1, 14109 Berlin, Germany*
[2]*Dahlem Center for Complex Quantum Systems and Fachbereich Physik, Freie Universität Berlin, Arnimallee 14, 14195 Berlin, Germany*
[3]*Institute of Physics, University of Bonn, Nussallee 12, 53115 Bonn, Germany*
[4]*Department of Physics and Astronomy, University of Waterloo, Waterloo, Ontario N2L 3G1, Canada*
[5]*Department of Physics, University of Windsor, 401 Sunset Avenue, Windsor, Ontario N9B 3P4, Canada*
[6]*Institute for Theoretical Solid State Physics, IFW Dresden and Würzburg-Dresden Cluster of Excellence ctd.qmat, Helmholtzstr. 20, 01069 Dresden, Germany*
[7]*Institut für Festkörperforschung, Technische Universität Berlin, 10623 Berlin, Germany*
[8]*Waterloo Institute for Nanotechnology, University of Waterloo, Waterloo, Ontario N2L 3G1, Canada*

(Dated: May 19, 2026)

S1. Energy expansion of the quartic perturbation

In this section, we present the series expansion of the energy for a spiral state perturbed by a perpendicular perturbation with wave vector $\boldsymbol{Q}_{\mathrm{aB}}$ in both the square and cubic lattices, demonstrating the quartic dependence of the energy of such a state on the perturbation amplitude.

A. Square lattice

To illustrate how quartic modes emerge in a spiral ground state perturbed by a perpendicular perturbation with a wave vector corresponding to the non-selected spiral, $\boldsymbol{Q}_{\mathrm{aB}}$, we consider a generic spiral with period L. First, it is useful to rewrite the perturbed state given in Eq. (3) of the main text as:

$$\boldsymbol{S}_i^{\text{quartic}} = \frac{1}{\sqrt{1+\delta^2\cos^2\left(\frac{2\pi}{L}x\right)}} \begin{pmatrix} \cos\left(\frac{2\pi}{L}y\right) \\ \sin\left(\frac{2\pi}{L}y\right) \\ \delta\cos\left(\frac{2\pi}{L}x\right) \end{pmatrix}, \tag{S1}$$

where the position of site i is given by $\boldsymbol{r}_i = (x, y)$ and we set $\boldsymbol{Q}_{\mathrm{B}} = (0, 2\pi/L)$, $\boldsymbol{Q}_{\mathrm{aB}} = (2\pi/L, 0)$. Furthermore, we have set the arbitrary phases to be $\phi = \phi' = 0$. Next, consider the energy term associated with the nth nearest-neighbor interactions:

$$J_n \sum_i \sum_{j\in n^{\text{th}}\text{ n.n of } i} \boldsymbol{S}_i \cdot \boldsymbol{S}_j. \tag{S2}$$

This term is proportional to the scalar product between the spin at site $\boldsymbol{r}_i = (x, y)$ and its n^{th} nearest neighbors, given by $\boldsymbol{r}_j = (x \pm a, y \pm b)$ and $(x \pm b, y \pm a)$. To avoid double counting, we include only one term from each pair related by a global minus sign: $(x + a, y + b)$, $(x - a, y + b)$, $(x - b, y + a)$, and $(x - b, y - a)$. These four terms form two pairs related by a 90° rotational symmetry around the $\hat{\boldsymbol{z}}$ axis. To show that the quadratic term vanishes, it is sufficient to consider one such pair, summed over the entire lattice:

$$\sum_{x,y} \boldsymbol{S}(x, y) \cdot \boldsymbol{S}(x + a, y + b) + \boldsymbol{S}(x, y) \cdot \boldsymbol{S}(x - b, y + a). \tag{S3}$$

Expanding the scalar products in a series of δ, we obtain for the second-order terms the following expression:

$$\begin{aligned} &\sum_{x,y} \delta^2 \cos\left(\frac{2\pi}{L}x\right)\left[\cos\left(\frac{2\pi}{L}(x+a)\right) + \cos\left(\frac{2\pi}{L}(x-b)\right)\right] \\ &\quad - \frac{\delta^2}{2}\cos\left(\frac{2\pi}{L}b\right)\left[\cos^2\left(\frac{2\pi}{L}(x+a)\right) + \cos^2\left(\frac{2\pi}{L}x\right)\right] \\ &\quad - \frac{\delta^2}{2}\cos\left(\frac{2\pi}{L}a\right)\left[\cos^2\left(\frac{2\pi}{L}(x-b)\right) + \cos^2\left(\frac{2\pi}{L}x\right)\right]. \end{aligned} \tag{S4}$$

Using algebraic manipulations and the fact that summing over the entire lattice causes terms proportional to $\cos\left(\frac{2\pi}{L}x\right)$ and $\sin\left(\frac{2\pi}{L}x\right)$, or equivalent expressions for y, to vanish, we arrive at:

$$\sum_{x,y} \frac{\delta^2}{2} \cos\left(\frac{4\pi}{L}x\right)\left[\cos\left(\frac{2\pi}{L}b\right)\sin^2\left(\frac{2\pi}{L}a\right)+\sin\left(\frac{2\pi}{L}b\right)\cos^2\left(\frac{2\pi}{L}a\right)\right]=0. \tag{S5}$$

This final expression vanishes when summing over the entire lattice. Therefore, while the existence of a spiral ground state depends on the Hamiltonian, the quartic nature of the mode involving a perpendicular perturbation with the wave vector of the non-selected spiral is a general property of the spiral ground state, independent of the specific Hamiltonian. The same argument also applies to two-dimensional spirals.

The energy expansion up to the fourth order for the state in Eq. (S1), specific to the square lattice discussed in the main text, is given by

$$e(\delta)=\sum_{i=1}^{3} e_i(\delta) \approx -1.00729 + 0.03906\delta^4 + O(\delta^6), \tag{S6}$$

where e_i with $i = 1, 2, 3$ are the energy contributions from the different lattice bonds with couplings J_1, J_2, J_3, respectively.

B. Cubic lattice

To compute the energy expansion, we consider a state similar to the one in Eq. (S1), generalized to the equal superposition of the two quartic perturbations $S_i^z \sim \delta[\cos(\boldsymbol{Q}_{\mathrm{aB}_1}\cdot\boldsymbol{r}_i)+\cos(\boldsymbol{Q}_{\mathrm{aB}_2}\cdot\boldsymbol{r}_i)]$. We rewrite the state as:

$$\boldsymbol{S}_i^{\text{quartic}} = \frac{1}{\sqrt{1+\delta^2(\cos^2\left(\frac{2\pi}{L}x\right)+\cos^2\left(\frac{2\pi}{L}z\right))}} \begin{pmatrix} \cos\left(\frac{2\pi}{L}y\right) \\ \sin\left(\frac{2\pi}{L}y\right) \\ \delta(\cos\left(\frac{2\pi}{L}x\right)+\cos\left(\frac{2\pi}{L}z\right)) \end{pmatrix}, \tag{S7}$$

where $\boldsymbol{r}_i = (x, y, z)$, $\boldsymbol{Q}_{\mathrm{B}} = (0, \frac{2\pi}{L}, 0)$, $\boldsymbol{Q}_{\mathrm{aB}_1} = (\frac{2\pi}{L}, 0, 0)$, and $\boldsymbol{Q}_{\mathrm{aB}_2} = (0, 0, \frac{2\pi}{L})$. To show that the terms proportional to δ^2 in the expression in Eq. (S2) vanish, the procedure is analogous to the one presented for the square lattice. The only difference in the cubic lattice case is that we must consider three contributions, as the perturbation consists of two terms. Specifically, the scalar product is taken between the spin at site $\boldsymbol{r}_i = (x, y, z)$ and three of its n^{th} nearest neighbors: (1) the spin at $(x + a, y + b, z + c)$ (2) the spin at $(x - b, y + a, z + c)$ obtained by a 90° rotation around the $\hat{\boldsymbol{z}}$-axis (3) the spin at $(x + a, y - c, z + b)$ obtained by a 90° rotation around the $\hat{\boldsymbol{x}}$-axis.

The energy expansion up to the fourth order for the state in Eq. (S7), specific to the cubic lattice discussed in the main text, is given by

$$e(\delta) = e_1(\delta) + e_2(\delta) + e_4(\delta) \approx -1.48114 + 0.153863\delta^4 + O(\delta^6). \tag{S8}$$

S2. Details on the Monte Carlo simulations

To generate the spin configurations needed for the spin Molecular Dynamics (sMD) simulations, we perform classical Monte Carlo (cMC) calculations on the square and cubic lattices. We use a particular version of the single-spin update algorithm called the adaptive Gaussian step algorithm, which allows for a controlled and fixed 50% acceptance ratio at all temperatures [S1]. Additionally, for each spin-update trial, we perform two over-relaxation steps. Then, at a given temperature, we perform 5×10^5 cMC steps consisting each of N single-spin update trials and $2N$ over-relaxation steps, where N is the number of spins in the system. Data for measurements is collected during the second half of the cMC steps.

For both lattices, we perform two types of simulations: cooling down and heating, both with logarithmic temperature steps. For the cooling-down simulations, we do 120 temperature steps from $T/J = 2$ down to $T/J = 0.01$, where J is the largest coupling. Then we perform an extra 31 steps down to $T/J = 10^{-12}$. For the heating simulations, we depart from a ground-state configuration and perform 34 logarithmic steps from $T/J = 10^{-12}$ up to 10^{-1} (16 steps in the cubic case). We save the last configuration at each temperature as a benchmark point.

From each configuration at a desired temperature, we generate 120 new spin configurations for the Molecular Dynamics simulations. This is done by performing 5×10^5 cMC steps between spin configurations, implying 60 million cMC steps between the first and last spin configurations at a given temperature.

In the case of the square lattice, we do this for $N = L^2$ lattices with $L = 20$, 40, 60, and 80. In the case of the cubic lattice, we do this for $N = L^3$ lattices with $L = 5$, 10, 15, and 20. In both cases, we use periodical boundary conditions, which do not frustrate the 5-site spiral ground state.

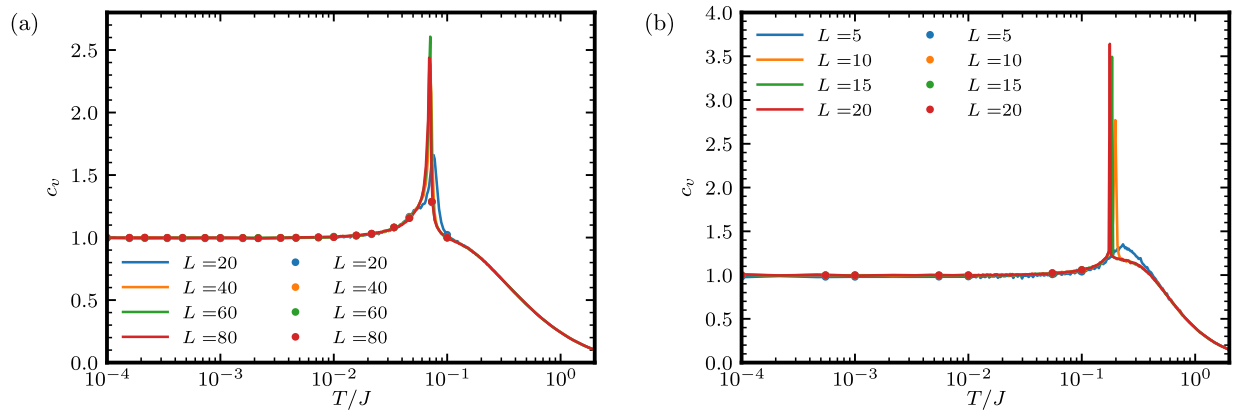

FIG. S1. Classical Monte Carlo calculations for the specific heat $c_v(T)$. The data from the cooling down simulations is shown in a continuous line, while the results from heating up are shown by the full dots. The temperature is shown in T/J, where J is the largest coupling in each case. Panels (a) and (b) correspond to the square and cubic lattice models, respectively.

For completeness, we show in Fig. S1 the specific heat $c_v(T)$ from the cMC calculations; in panel (a) for the square lattice model and in panel (b) for the cubic lattice. In both cases, the lines indicate the calculations for the cooling down simulations, while the dots are the results for the heating up simulations, noting an excellent agreement between both. Also, both calculations find evidence for only a single phase transition into a spiral phase.

S3. Details on the spin Molecular Dynamics simulations

In this section, we explain how the spin Molecular Dynamics (sMD) simulations are performed and how the dynamical structure factor is computed within this framework.

A. Overview of the method and numerical details

The sMD simulations consist of numerically integrating the classical equations of motion for the spins:

$$\frac{d\boldsymbol{S}_i}{dt} = \boldsymbol{S}_i \times \boldsymbol{h}_i, \tag{S9}$$

where $\boldsymbol{h}_i = -\frac{\partial H}{\partial \boldsymbol{S}_i}$ is the local effective field acting on $\boldsymbol{S}_i$, arising from interactions with neighboring spins. These equations correspond to the Landau-Lifshitz equations without the damping term [S2]. The numerical integration is carried out using the Runge-Kutta Cash-Karp method, implemented through the Boost C++ Library [S3].

B. Computing the dynamical structure factor

The central quantity of our study is the dynamical structure factor

$$\mathcal{S}(\boldsymbol{q},\omega) = \frac{1}{2\pi N}\sum_{i,j=1}^{N}\int_{-\infty}^{\infty} e^{i\omega t} e^{-i\boldsymbol{q}(\boldsymbol{r}_i-\boldsymbol{r}_j)}\langle \boldsymbol{S}_i(0)\cdot\boldsymbol{S}_j(t)\rangle dt \tag{S10}$$

evaluated at $\boldsymbol{q} = \boldsymbol{Q}_{\rm aB}$. To compute $\mathcal{S}(\boldsymbol{Q}_{\rm aB},\omega)$, we follow the approach of Ref. [S4]. Specifically, the spin Fourier transform for each spin component is computed during the simulation. At the end of the time evolution, $\mathcal{S}(\boldsymbol{Q}_{\rm aB},\omega)$ is obtained by multiplying the Fourier transform by its complex conjugate and summing over the components. For the calculation of $\mathcal{S}(\boldsymbol{Q}_{\rm aB},\omega)$ at finite temperature, the results are obtained by averaging over 120 simulations. Each simulation starts from an independent, equilibrated MC configuration, which is obtained by heating up the system starting from zero temperature.

S4. Fitting procedures

In this section, we describe the fitting procedures used in this work. First, we explain how the gap value is extracted from the dynamical structure factor. Then, we discuss how these extracted values are fitted using the function in Eq. (6) of the main text, which is derived from the phenomenological model. The results of the second fit are shown in Figs. 2(b) and 2(c).

A. Gap extraction from the dynamical structure factor

The value of the gap at $\boldsymbol{q} = \boldsymbol{Q}_{\mathrm{aB}}$ is obtained by fitting $\mathcal{S}(\boldsymbol{Q}_{\mathrm{aB}}, \omega)$ with a Lorentzian function multiplied by a scaling factor A:

$$f(x) = A\frac{\gamma}{\pi[\gamma^2 + (x - x_0)^2]}. \tag{S11}$$

The value of the gap corresponds to the position of the maximum, given by x_0. For each linear size and temperature, we compute the difference between the gap value extracted from the fit and the position of the maximum of $\mathcal{S}(\boldsymbol{Q}_{\mathrm{aB}}, \omega)$. Since all observed differences lie within $3\gamma/4$ (square lattice) and $\gamma/2$ (cubic lattice), we adopt these values as estimates of the error.

B. Fitting the simulated gaps

The gap values are fitted using the function in Eq. (6) of the main text, which describes the gap behavior derived from the phenomenological model. At low temperatures, this function predicts $\Delta \sim T^{1/4}$. This scaling is confirmed by the linear fit of $\log T$ versus $\log \Delta$, shown by the blue line in Fig. 2(b) for the square lattice and the blue line in Fig. 2(c) for the cubic lattice. Thus, we verify that the function in Eq. (6) provides a good fit to the data at low temperatures. Starting from the lowest temperatures, we gradually increase the number of data points used in the fit. For each step, we compute χ^2/df, where $\mathrm{df} = n - 2$ is the number of degrees of freedom (with n being the number of points used, minus two since the fit depends on two parameters). We then compare χ^2/df with the chi-squared critical value at a 95% confidence level, denoted as $\chi^2_{0.05}/\mathrm{df}$. The computed χ^2/df values and corresponding critical values for the two lattices are shown in Fig. S2. The fits presented in Figs. 2(b) and 2(c) correspond to the maximum number of points where χ^2/df remains below the critical threshold across all linear system sizes. This results in $n = 19$ for the square lattice and $n = 8$ for the cubic lattice.

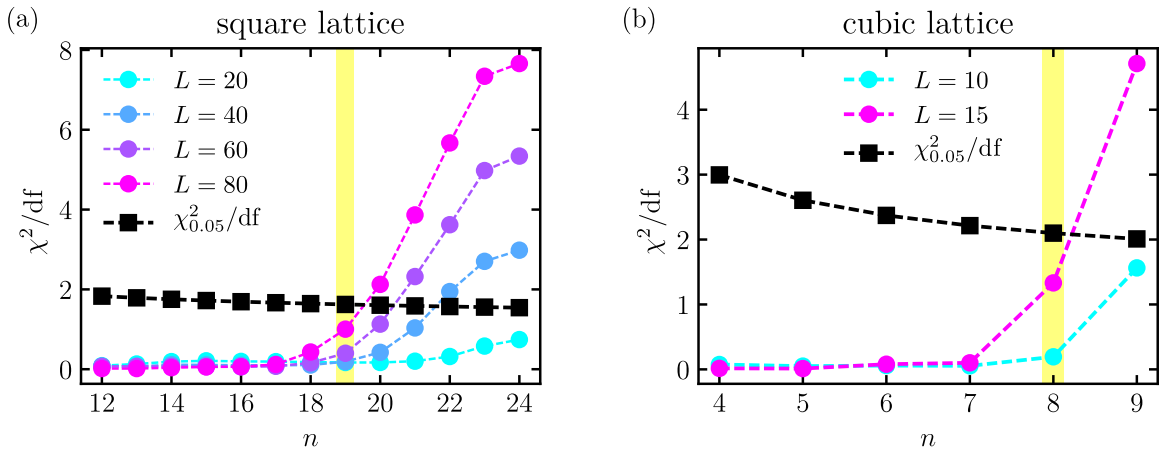

FIG. S2. (a) The reduced chi-squared per degree of freedom, χ^2/df, as a function of n, the number of points used to fit the gap values with the function in Eq. (6), for the square lattice with $L = 20, 40, 60, 80$. Since this function depends on two parameters, the degrees of freedom are given by $n - 2$. The black squares represent the critical value $\chi^2_{0.05}/\mathrm{df}$. The yellow region highlights the maximum number of points for which χ^2/df remains below the critical chi-squared value for all system sizes. These selected points, starting from the lowest-temperature point, are those used in the fit shown in Fig. 2(b) of the main text. (b) Same as (a) for the cubic lattice, with $L = 10, 15$.

S5. Additional data

In this section, we present additional data for the square and cubic lattices. Specifically, the energy gap as a function of the perturbation strength, and the gap as a function of temperature at the two anti-Bragg wave vectors.

A. Square lattice

The quartic perturbation is energetically softer than all other possible deformations of the ground state (apart from global spin rotations). Therefore, we can alternatively access the low-temperature behavior by initializing the system precisely in the exact perturbed state (see main text), and then obtain its dynamics via sMD for varying perturbation strengths δ. The sMD results for the 2D model then show that the dynamical spin structure factor $\mathcal{S}(\boldsymbol{Q}_{\mathrm{aB}}, \omega)$ at the anti-Bragg point is gapped and the gap Δ scales linearly with the perturbation strength, $\Delta \sim \delta$ (see Fig. S3). Based on this result, we can infer the temperature dependence of the gap by considering that the energy for a quartic mode is $E \sim \delta^4$, and $E \sim T$ by the principle of equipartition. Thus, we find that $\delta \sim T^{1/4}$ yields a gap that scales as $\Delta \sim T^{1/4}$ in agreement with the dimensional analysis presented in the main text.

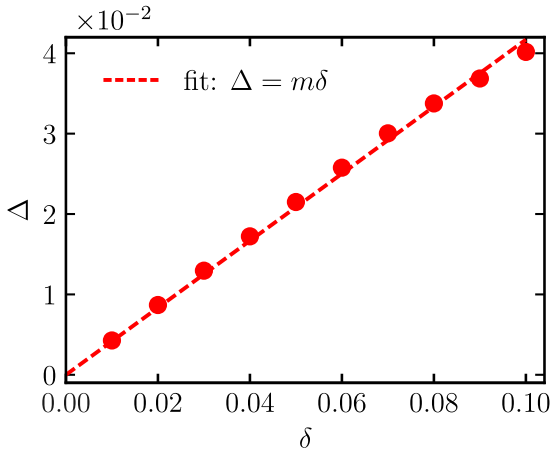

FIG. S3. Gap computed as the maximum of $\mathcal{S}(\boldsymbol{Q}_{\mathrm{aB}}, \omega)$ as a function of the perturbation strength δ for the 2D model. The data are fitted with a linear function ($m \approx 0.4$).

B. Cubic lattice

Similarly to the square lattice discussed above, we compute $\mathcal{S}(\boldsymbol{Q}_{\mathrm{aB}}, \omega)$, starting from a configuration in which the quartic modes are excited directly, using the expression in Eq. (S7). The sMD simulations show that $\mathcal{S}(\boldsymbol{Q}_{\mathrm{aB}_1}, \omega)$ and $\mathcal{S}(\boldsymbol{Q}_{\mathrm{aB}_2}, \omega)$ display a peak at the same frequency, that scales linearly with δ, see Fig. S4.

As explained in the main text, the cubic lattice exhibits quartic modes at the two not-selected spiral wave vectors denoted as $\boldsymbol{Q}_{\mathrm{aB}_1}$ and $\boldsymbol{Q}_{\mathrm{aB}_2}$. As shown in Fig. S5, the gap at $\boldsymbol{Q}_{\mathrm{aB}_1}$ and $\boldsymbol{Q}_{\mathrm{aB}_2}$ is the same, which agrees with the equivalence of these points. This agreement further confirms that the initial configurations are equilibrated correctly. In Fig. 2(c) of the main text, the gap values are obtained from the average of the gaps at the two anti-Bragg points.

S6. Frequency of the quartic oscillator in the presence of the entropic term

We consider a phenomenological model of a quartic oscillator with an additional entropic contribution, described by the effective Hamiltonian

$$H_{\mathrm{eff}} = \frac{p^2}{2m} + \lambda x^4 + \alpha T x^2, \tag{S12}$$

where the first two terms are energetic contributions and the last term arises from entropy (see the main text). To estimate the frequency of this oscillator, we apply a mean-field decoupling of the quartic term as $x^4 \approx 6 \langle x^2 \rangle x^2$, where $\langle \cdots \rangle$ denotes thermal

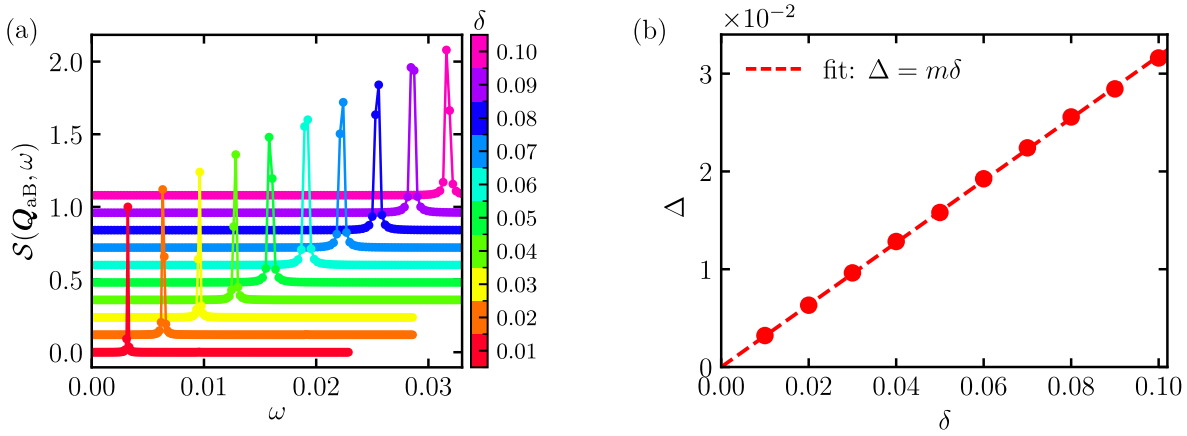

FIG. S4. (a) Normalized dynamical structure factor $\mathcal{S}(\boldsymbol{q},\omega)$ at $\boldsymbol{q} = \boldsymbol{Q}_{\rm aB}$ for different values of the perturbation strength δ, obtained from sMD simulations for $L = 15$. The calculation is performed at both $\boldsymbol{Q}_{\rm aB_1}$ and $\boldsymbol{Q}_{\rm aB_2}$, and since the resulting curves are identical, we use the notation $\boldsymbol{Q}_{\rm aB}$ in the plot to represent both points. (b) Gap Δ at $\boldsymbol{q} = \boldsymbol{Q}_{\rm aB_1}$, equal to the one at $\boldsymbol{q} = \boldsymbol{Q}_{\rm aB_2}$, as a function of the perturbation strength δ. The data are fitted with a linear function ($m \approx 0.32$).

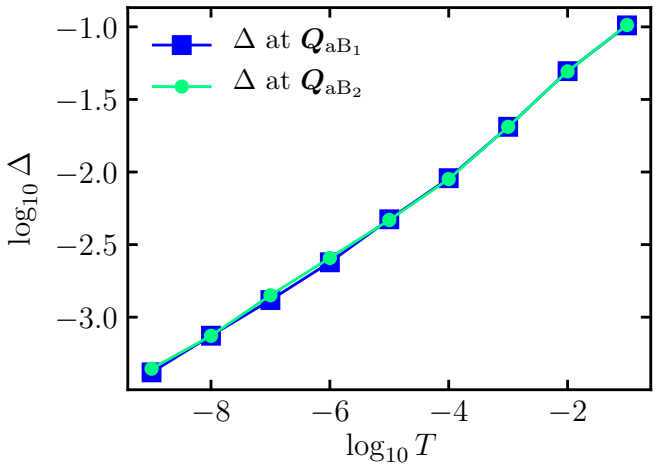

FIG. S5. Values of the gap Δ as a function of temperature, extracted respectively from $\mathcal{S}(\boldsymbol{Q}_{\rm aB_1},\omega)$ and $\mathcal{S}(\boldsymbol{Q}_{\rm aB_2},\omega)$, for the cubic system with linear size $L = 15$.

average, assuming thermal equilibrium at temperature T. The factor of 6 comes from the number of ways to contract x^4 into a product involving $\langle x^2\rangle\, x^2$. This decoupling leads to an effective quadratic Hamiltonian

$$H_{\rm quad} \approx \frac{p^2}{2m} + \left(6\lambda\langle x^2\rangle + \alpha T\right) x^2. \tag{S13}$$

For such a quadratic Hamiltonian, the thermal average

$$\langle x^2\rangle = \frac{T}{m\omega^2} = \frac{T}{2\left(6\lambda\langle x^2\rangle + \alpha T\right)}. \tag{S14}$$

This equation can be solved self-consistently for $\langle x^2\rangle$ to find the frequency ω or, alternatively, one may rewrite Eq. (S14) as

$$\frac{m\omega^2}{2} = \frac{6\lambda T}{m\omega^2} + \alpha T. \tag{S15}$$

This is a quadratic equation in ω, giving

$$\omega = \sqrt{\frac{\alpha T}{m}}\left(1 + \sqrt{1 + \frac{2\,T^*}{T}}\right)^{1/2}, \tag{S16}$$

where $T^* = 6\lambda/\alpha^2$. This frequency is identified as the thermal gap Δ of the quartic mode at temperature T.

S7. Derivation of the phenomenological model

To derive the phenomenological quartic oscillator model from the microscopic spin Hamiltonian, we start from a different representation of the classical spins:

$$\begin{aligned}\boldsymbol{S}_i = &\sqrt{1-\frac{1}{4}(x_i^2+p_i^2)}\, x_i\, \hat{\boldsymbol{x}}_i + \sqrt{1-\frac{1}{4}(x_i^2+p_i^2)}\, p_i\, \hat{\boldsymbol{y}}_i \\ &+ \left[1-\frac{1}{2}(x_i^2+p_i^2)\right] \hat{\boldsymbol{z}}_i,\end{aligned} \tag{S17}$$

where the real variables x_i, p_i satisfy the Poisson bracket relation $\{x_i, p_j\} = \delta_{ij}$, and $\{\hat{\boldsymbol{x}}_i, \hat{\boldsymbol{y}}_i, \hat{\boldsymbol{z}}_i\}$ is any right-handed *local* orthogonal coordinate frame [S5]. This representation, together with the Poisson bracket relation of x_i and p_i reproduces the canonical Poisson bracket for spin components $\{S_i^\eta, S_j^\rho\} = \delta_{ij}\sum_\sigma \epsilon_{\eta\rho\sigma} S_i^\sigma$. We further choose the local frame $\{\hat{\boldsymbol{x}}_i, \hat{\boldsymbol{y}}_i, \hat{\boldsymbol{z}}_i\}$ to be aligned with the ground-state spiral ordering at wave vector $\boldsymbol{Q}_{\mathrm{B}}$

$$\begin{aligned}\hat{\boldsymbol{x}}_i &= -\sin(\boldsymbol{Q}_{\mathrm{B}}\cdot\boldsymbol{r}_i)\,\hat{\boldsymbol{x}} + \cos(\boldsymbol{Q}_{\mathrm{B}}\cdot\boldsymbol{r}_i)\,\hat{\boldsymbol{y}}, \\ \hat{\boldsymbol{y}}_i &= \hat{\boldsymbol{z}}, \\ \hat{\boldsymbol{z}}_i &= \cos(\boldsymbol{Q}_{\mathrm{B}}\cdot\boldsymbol{r}_i)\,\hat{\boldsymbol{x}} + \sin(\boldsymbol{Q}_{\mathrm{B}}\cdot\boldsymbol{r}_i)\,\hat{\boldsymbol{y}},\end{aligned} \tag{S18}$$

where $\{\hat{\boldsymbol{x}}, \hat{\boldsymbol{y}}, \hat{\boldsymbol{z}}\}$ are the Cartesian directions in the *global* coordinate frame. Substituting Eqs. (S17) and (S18) into the microscopic spin Hamiltonians, Taylor expanding in x_i, p_i, and keeping terms up to quadratic order, yields the energy

$$H_2 = \frac{1}{2}\sum_{i,\nu} J_\nu \left[\cos(\boldsymbol{Q}_{\mathrm{B}}\cdot\boldsymbol{\nu})\left(x_i x_{i+\nu} - x_i^2 - p_i^2\right) + p_i p_{i+\nu}\right], \tag{S19}$$

where J_ν denotes the coupling strength on the bond $\boldsymbol{\nu}$ from the lattice site i. Further, considering the Fourier transform

$$x_i = \frac{1}{\sqrt{N}}\sum_{\boldsymbol{k}} e^{i\boldsymbol{k}\cdot\boldsymbol{r}_i} x_{\boldsymbol{k}}, \qquad p_i = \frac{1}{\sqrt{N}}\sum_{\boldsymbol{k}} e^{i\boldsymbol{k}\cdot\boldsymbol{r}_i} p_{\boldsymbol{k}}, \tag{S20}$$

with N being the number of spins in the system, we obtain

$$H_2 = \frac{1}{2}\sum_{\boldsymbol{k}} \left[L_{\boldsymbol{k}}\, x_{-\boldsymbol{k}} x_{\boldsymbol{k}} + M_{\boldsymbol{k}}\, p_{-\boldsymbol{k}} p_{\boldsymbol{k}}\right], \tag{S21}$$

where

$$\begin{aligned}L_{\boldsymbol{k}} &= \sum_\nu J_\nu \cos(\boldsymbol{Q}_{\mathrm{B}}\cdot\boldsymbol{\nu})\left(e^{i\boldsymbol{k}\cdot\boldsymbol{\nu}} - 1\right), \\ M_{\boldsymbol{k}} &= \sum_\nu J_\nu \left(e^{i\boldsymbol{k}\cdot\boldsymbol{\nu}} - \cos(\boldsymbol{Q}_{\mathrm{B}}\cdot\boldsymbol{\nu})\right).\end{aligned} \tag{S22}$$

In reciprocal space, we have the Poisson bracket $\{x_{\boldsymbol{k}}, p_{\boldsymbol{k}'}\} = \delta_{\boldsymbol{k}+\boldsymbol{k}'}$ which thus implies the conjugate variable to $x_{\boldsymbol{k}}$ is $p_{-\boldsymbol{k}}$. Therefore, the quadratic Hamiltonian in Eq. (S21) describes a simple harmonic oscillator with frequency $\omega_{\boldsymbol{k}} = \sqrt{L_{\boldsymbol{k}} M_{\boldsymbol{k}}}$. Thus, a zero mode occurs when $L_{\boldsymbol{k}} = 0$, $M_{\boldsymbol{k}} = 0$, or both are zero. We find $L_{\boldsymbol{0}} = 0$ and $M_{\boldsymbol{Q}_{\mathrm{B}}} = M_{\boldsymbol{Q}_{\mathrm{aB}}} = 0$. To focus on the mode at $\boldsymbol{Q}_{\mathrm{aB}}$, we retain only the wave vectors $\boldsymbol{Q}_{\mathrm{aB}}$ and $-\boldsymbol{Q}_{\mathrm{aB}}$ in the Fourier expansion (as conjugate variables appear at $\boldsymbol{k}$ and $-\boldsymbol{k}$):

$$\begin{aligned}x_i &= \frac{1}{\sqrt{N}}\left(e^{i\boldsymbol{Q}_{\mathrm{aB}}\cdot\boldsymbol{r}_i} x_{\boldsymbol{Q}_{\mathrm{aB}}} + e^{-i\boldsymbol{Q}_{\mathrm{aB}}\cdot\boldsymbol{r}_i} x_{-\boldsymbol{Q}_{\mathrm{aB}}}\right), \\ p_i &= \frac{1}{\sqrt{N}}\left(e^{i\boldsymbol{Q}_{\mathrm{aB}}\cdot\boldsymbol{r}_i} p_{\boldsymbol{Q}_{\mathrm{aB}}} + e^{-i\boldsymbol{Q}_{\mathrm{aB}}\cdot\boldsymbol{r}_i} p_{-\boldsymbol{Q}_{\mathrm{aB}}}\right).\end{aligned} \tag{S23}$$

The real valuedness of x_i and p_i implies the complex conjugate $x^*_{-\boldsymbol{k}} = x_{\boldsymbol{k}}$ and $p^*_{-\boldsymbol{k}} = p_{\boldsymbol{k}}$ for any $\boldsymbol{k}$. Making use of these conditions and the relation $\{x_{\boldsymbol{k}}, p_{\boldsymbol{k}'}\} = \delta_{\boldsymbol{k}+\boldsymbol{k}'}$, we rewrite the Fourier components as the following

$$\begin{aligned}x_{\boldsymbol{Q}_{\mathrm{aB}}} &= (X + i\tilde{P})/\sqrt{2}, \quad x_{-\boldsymbol{Q}_{\mathrm{aB}}} = (X - i\tilde{P})/\sqrt{2}, \\ p_{\boldsymbol{Q}_{\mathrm{aB}}} &= (P - i\tilde{X})/\sqrt{2}, \quad p_{-\boldsymbol{Q}_{\mathrm{aB}}} = (P + i\tilde{X})/\sqrt{2},\end{aligned} \tag{S24}$$

where X, P and $\tilde{X}, \tilde{P}$ satisfy the Poisson bracket relations $\{X, P\} = \{\tilde{X}, \tilde{P}\} = 1$, and other Poisson brackets are zero. Eq. (S23) then becomes

$$x_i = \sqrt{\frac{2}{N}} \left(X \cos(\boldsymbol{Q}_{\mathrm{aB}} \cdot \boldsymbol{r}_i) - \tilde{P} \sin(\boldsymbol{Q}_{\mathrm{aB}} \cdot \boldsymbol{r}_i) \right),$$
$$p_i = \sqrt{\frac{2}{N}} \left(P \cos(\boldsymbol{Q}_{\mathrm{aB}} \cdot \boldsymbol{r}_i) + \tilde{X} \sin(\boldsymbol{Q}_{\mathrm{aB}} \cdot \boldsymbol{r}_i) \right). \tag{S25}$$

Substituting Eq. (S25) into Eq. (S17), Taylor expanding it up to quartic order in $X, P, \tilde{X}, \tilde{P}$, and then inserting the expansion in the microscopic spin Hamiltonian yields an effective quartic oscillator Hamiltonian, which includes several quartic (momentum-conserving) combinations of those four variables. Most importantly, these quartic terms in the Hamiltonian have an explicit system-size dependence, which is $O(1/N)$; Eq. (S25) shows that each quartic term is $O(1/N^2)$, with the microscopic spin Hamiltonian having a sum over bonds, which gives a contribution of $O(N)$ – combining these contributions, we ultimately get a $1/N$ coefficient for the quartic terms in the final effective quartic Hamiltonian. We thus see that the prefactor of the quartic potential term in Eq. (5) of the main text scales as $\lambda \sim 1/N$.

With the proper N-dependent scaling of the effective quartic Hamiltonian in reciprocal space at hand, proceeding next with a mean-field decoupling of the quartic terms as done for Eq. (5) in the main text, yields an effective simple harmonic oscillator whose frequency – and hence the gap Δ – has the same form as in Eq. (6) from the main text, with the crossover temperature $T^* \sim 1/N$. Thus, the gap at low temperatures behaves as $\Delta \sim (T/N)^{1/4}$, while at high temperatures, where the entropic contribution dominates, $\Delta \sim \sqrt{T}$ — independent of the system size. Consequently, in the thermodynamic limit ($N \to \infty$), $T^* \to 0$ and only one scaling relation — $\Delta \sim \sqrt{T}$ — remains.

[S1] J. D. Alzate-Cardona, D. Sabogal-Suárez, R. F. L. Evans, and E. Restrepo-Parra, Optimal phase space sampling for Monte Carlo simulations of Heisenberg spin systems, Journal of Physics: Condensed Matter **31**, 095802 (2019).

[S2] L. D. Landau and E. Lifshitz, On the theory of the dispersion of magnetic permeability in ferromagnetic bodies, Phys. Z. Sowjetunion **8**, 101 (1935).

[S3] K. Ahnert and M. Mulansky, Boost C++ Library: Odeint (2012).

[S4] S. Zhang, H. J. Changlani, K. W. Plumb, O. Tchernyshyov, and R. Moessner, Dynamical Structure Factor of the Three-Dimensional Quantum Spin Liquid Candidate $NaCaNi_2F_7$, Phys. Rev. Lett. **122**, 167203 (2019).

[S5] This representation is a classical form [S6–S8] of the Holstein-Primakoff representation [S9] with unit spin length and $a_i = (x_i + ip_i)/\sqrt{2}$.

[S6] H. Suhl, The theory of ferromagnetic resonance at high signal powers, Journal of Physics and Chemistry of Solids **1**, 209 (1957).

[S7] E. Schlömann, Fine structure in the decline of the ferromagnetic resonance absorption with increasing power level, Phys. Rev. **116**, 828 (1959).

[S8] P. Krivosik and C. E. Patton, Hamiltonian formulation of nonlinear spin-wave dynamics: Theory and applications, Phys. Rev. B **82**, 184428 (2010).

[S9] T. Holstein and H. Primakoff, Field Dependence of the Intrinsic Domain Magnetization of a Ferromagnet, Phys. Rev. **58**, 1098 (1940).